ACS SENSORS

Article

Cite This: ACS Sens. XXXX, XXX, XXX−XXX

pubs.acs.org/acssensors

Dean Flow Assisted Single Cell and Bead Encapsulation for High Performance Single Cell Expression Profiling

Luoquan Li,[†,‡,§,#] Ping Wu,[‡,§,#] Zhaofeng Luo,[∥] Lei Wang,[‡,§] Weiping Ding,[⊥] Tao Wu,[‡,§] Jinyu Chen,[†] Jinlong He,[†] Yi He,[†] Heran Wang,[‡,§] Ying Chen,[¶] Guibo Li,[‡,§] Zida Li,*[,□] and Liqun He*[,†,▲]

[†]Department of Thermal Science and Energy Engineering, [∥]School of Life Sciences, and [⊥]Department of Electronic Science and Technology, University of Science and Technology of China, Hefei 230027, China

[‡]BGI-Shenzhen, Shenzhen 518083, China

[§]China National GeneBank, BGI-Shenzhen, Shenzhen 518120, China

[¶]School of Materials and Energy, Guangdong University of Technology, Guangzhou 510006, China

[□]Department of Biomedical Engineering, School of Medicine, Shenzhen University, Shenzhen 518060, China

[▲]Hefei Energy Research Institute, Hefei 230051, China

Supporting Information

ABSTRACT: Droplet microfluidics-based platform (Drop-seq) has been shown to be a powerful tool for single cell expression profiling. Nevertheless, this platform required the simultaneous encapsulation of single cell and single barcoded bead, the incidence of which was very low, limiting its efficiency. Spiral channels were reported to focus the barcoded beads and thus increased the efficiency, but focusing of cells was not demonstrated, which could potentially further enhance the performance. Here, we designed spiral and serpentine channels to focus both bead and cell solutions and implemented this microfluidic design on Drop-seq. We characterized the effect of cell/bead concentration on encapsulation results and tested the performance by coencapsulating barcoded beads and human−mouse cell mixtures followed by sequencing. The results showed ∼300% and ∼40% increase in cell utilization rate compared to the traditional Drop-seq device and the device focusing beads alone, respectively. This chip design showed great potential for high efficiency single cell expression profiling.

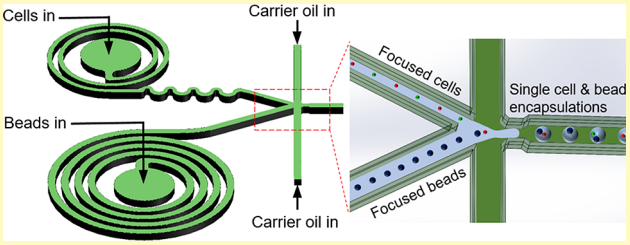

KEYWORDS: *inertial microfluidics, Dean flow, spiral channel, scRNA-seq, cell encapsulation, Drop-seq*

Conventional biological assays, such as qPCR and Western blot, are often performed at the bulk tissue level. Such assaying strategies assumed the overall tissue as a homogeneous entity and gauged the corresponding average values. Recently, it has been more and more appreciated that the heterogeneity of individual cells within a tissue has a non-negligible impact on the analysis of assay results.[1,2] Heterogeneous gene structure and gene expression status of individual cells have been revealed on the single cell level by whole genome sequencing,[3] transcriptome sequencing,[4,5] and epigenetic sequencing.[6] Single cell analysis has played a significant role in discovering unseen biological mechanisms,[7] as well as in making informed and personalized treatment plans in clinics.[8]

Single-cell transcriptome sequencing (scRNA-seq) gained great attention in recent years as a method for studying individual cell transcriptomes on a large scale.[9−12] It revealed in detail the gene expression of whole tissues and elucidated the genetic and epigenetic mechanisms.[13] Compared to conventional assays performed on bulk tissue level, scRNA-seq can quantify intrapopulation heterogeneity and dissect the transcriptional landscape of single cells at high resolution. In addition, scRNA-seq is important in the evaluation of genetically heterogeneous tumors, significantly impacting the battle against cancer.[14]

A major challenge in the transition from bulk tissue assay to single cell analysis lies in the techniques for efficient sample preparation, wherein microfluidics could serve as a powerful tool. Microfluidics is a technology that provides exquisite flow control with low sample consumption and dimensions comparable to single cell sizes. Along with the various available on-chip operation techniques, these advantages have made microfluidics an ideal tool for sample preparation in single cell analysis. Leveraging the advantages that microfluidics possesses, a few high-throughput single-cell analysis platforms have been developed.[15−18] In 2015, Macosko et al. reported a high-throughput scRNA-seq method based on droplet microfluidics (Drop-seq),[15] which encapsulated a single cell and a single barcoded bead into nanoliter droplets. The barcode of

Received: January 23, 2019
Accepted: April 24, 2019

DOI: 10.1021/acssensors.9b00171
ACS Sens. XXXX, XXX, XXX−XXX

each bead, appearing in the sequencing data, served as the identifier of individual cells and helped trace the origin of each read. This smart design offered the opportunity of parallel scRNA-seq and significantly reduced the bias in PCR amplification and noise in sequencing data analysis.

Despite the great potential that Drop-seq has shown, this platform has challenges. The nature of the experiment required a single cell and a single bead being simultaneously encapsulated in a single droplet and strictly prohibited encapsulation of multiple cells and multiple beads. The encapsulation incidence followed Poisson distribution; to minimize multiple encapsulation, the cell/bead suspension needed to be highly diluted. As a result, the encapsulation rate was reported to be as low as 0.15% under low cell/bead concentration of 100 μL^{-1} (ref 15). Suboptimal encapsulation rate inevitably compromised the efficiency and the throughput of the platform, which is particularly problematic in experiments where cells of interests are scarce.

Inertial focusing[19,20] provides a way to hydrodynamically localize particles in certain regions of the channel cross section. Consequently, particles line up and approach the encapsulation region one by one, thus reducing the incidence of multiple encapsulation and improving the encapsulation efficiency. When particles flow in microfluidic channels, due to the parabolic velocity profile, they are subjected to lift forces, namely, shear gradient lift force and wall effect lift force. In curved channels, the inertia of the fluids generates secondary swirling flow, named Dean flow, which accelerates the lateral displacement of the particles and thus facilitates the focusing. Based on the principle of inertial focusing, spiral channels were adopted in a reported work to order barcoded beads before droplet encapsulation,[21] leading to Drop-seq with improved performance. It was reported that cell utilization rate of 20% was achieved and the throughput was improved.

Despite that, cell focusing was not implemented in the reported work, likely due to cells' small size that made focusing challenging. By focusing cells along with beads, the performance of Drop-seq could be further improved. To this end, here we developed a new microfluidic chip which inertially ordered both beads and cells, aiming for high efficiency single cell expression profiling. In particular, we incorporated serpentine channels as well as spiral channels before the droplet generation region to effectively focus cells and beads. We investigated the effect of cell/bead concentration on the focusing results and encapsulation efficiency, and we tested the utility of this platform by performing single cell mRNA sequencing of human−mouse cell mixture. The results showed that our device possessed good performance efficiency even when operating at a high cell concentration of 300 μL^{-1} and high bead concentration of 900 μL^{-1}, and cell utilization rate of nearly 29% was achieved, which was ∼300% and ∼40% higher than the traditional Drop-seq device and the device implemented only bead focusing. Our platform showed great potential for single cell expression profiling with improved efficiency.

MATERIALS AND METHODS

Bead Preparation. Plain beads without surface functionalization (CM-300-10 and CM-100-10, Spherotech Inc., USA) with diameters of 10 and 30 μm were used in lieu of cells and barcoded beads, respectively, to test encapsulation efficiencies. 10 μm latex beads functionalized with fluorophore (PN 6602796, Beckman Coulter, USA) were used to assist visualization. The density of the bead solution was adjusted to 1.15 g/mL by supplementing OptiPrep Density Gradient Medium (D1556, Sigma-Aldrich, USA) with 10:3 volume-to-volume ratio to alleviate bead sedimentation.

Barcoded beads (OSKO-2011-10, ChemGenes Corp., USA) functionalized with primers were used to capture mRNA released from lysed cells in the Drop-seq experiment. The primers on each bead consist of a common PCR sequence, an identical cell barcode, varied unique molecular identifiers (UMIs), and a poly-T tail. Upon delivery, the beads were gently washed twice with 100% ethanol to remove free nucleotide sequences, before being washed and resuspended in TE/TW buffer (TE Buffer pH 8.0, 0.01% Tween). The suspension was then filtered through a 100 μm filter (BD Falcon, BD BioSciences, USA) to remove aggregates and the filtrates were aliquoted into multiple tubes for future use. Beads were stored strictly between 3.5 and 4 °C. Before each experiment, the beads were resuspended in lysis buffer containing 200 mM Tris, pH 7.5, 6% Ficoll PM-400 (17-0300-10, GE Healthcare, Sweden), 0.2% sarcosyl (L7414, Sigma, USA), and 20 mM EDTA. Dithiothreitol was supplemented to the lysate prior to droplet generation.

Cell Preparation. Two cell lines (Human HEK293T and Mouse NIH3T3) were used. Cells were cultured in high-glucose Dulbecco's Modified Eagle's medium (DMEM; Gibco, Fisher Scientific, USA) supplemented with 10% (v/v) fetal bovine serum (Gibco, Fisher Scientific, USA) and 1% penicillin−streptomycin antibiotics (Invitrogen, USA). Cells were passaged at a confluency of about 75%.

Microfluidic Devices. The chip design adopted spiral channels and serpentine channels following the inlets to focus cells/beads, as shown in Figure 1a. The microfluidic chip was fabricated with

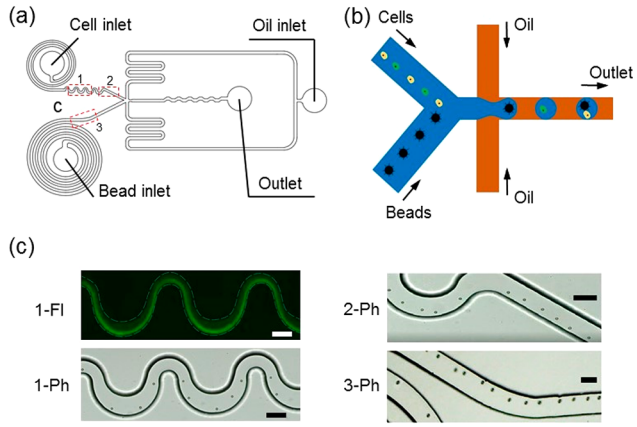

Figure 1. (a) Schematic of the design of the microfluidic chip. Spiral channels were adopted for bead focusing; due to the small size of cells, serpentine channels were added to achieve cell focusing. (b) Schematic showing the droplet generation and bead/cell encapsulation. Focused cell/bead flows led to improved efficiency of bead/cell encapsulation. (c) Fluorescent (Fl) and phase contrast (Ph) micrographs showing the position of cells/beads in the microfluidic channels at various locations as indicated in Figure 1a. The fluorescent micrograph was exposed relatively longer to visualize the particle trajectories. Scale bars, 100 μm.

standard soft lithography and the mold was fabricated using SU-8 photolithography. Polydimethylsiloxane (PDMS; Sylgard 184, Dow Corning, USA) with 10:1 base-to-curing agent ratio was poured on the mold and degassed for about 10 min, before it was baked in 80 °C oven for 40 min to cure. After baking, the PDMS was peeled off from the wafer and cut with razor blades. Biopsy punches were used to punch holes for tubing connection. Finally, the PDMS slab was bonded to glass slide after surface activation with oxygen plasma (Harrick Plasma, USA) followed by another baking at 80 °C. The channels were rendered hydrophobic by treating with Aquapel.

The chip design incorporated three inlets, namely, cell, bead, and carrier oil inlet, and one outlet. The chip had three functional units: two spiral structures with serpentine channels for cell/bead ordering,

DOI: 10.1021/acssensors.9b00171
ACS Sens. XXXX, XXX, XXX−XXX

a droplet generator (Figure 1b), and a serpentine channel for efficient mixing of generated droplets. The chip had a height of 120 μm throughout. Cell channel was a 2-loop spiral channel with a width of 80 μm. The innermost layer has a radius of 740 μm, and the interval between adjacent two loops was 100 μm. The spiral channel was followed by an asymmetric serpentine channel, with small curvature radius of 40 and 100 μm and large curvature radius of 93.5 and 150 μm. The bead channel was 5-loop spiral channel with a radius of 760 μm for the innermost layer, 100 μm intervals between adjacent loops, and 120 μm channel width. The detailed chip dimension can be found in Figure S1 a and b.

Droplet Generation and Cell/Bead Encapsulation. Cells were suspended in PBS supplemented with 0.01% BSA (v/v) and beads were suspended in lysis agent. The bead/cell suspensions were stored in 1.5 mL centrifuge tubes and connected to the chip via polyethylene tubing (BB31695-PE/2, Scientific Commodities Inc.). Droplets were collected in a customized centrifuge tube with inlet and outlet on the lid. The outlet was connected to a syringe pump, which was set on withdrawal mode with a typical flow rate of 30 mL/h to maintain the negative pressure and form droplets stably,[22,23] as shown in Figure S1c. An inverted microscope (IX71, Olympus, Germany), coupled with a high-speed camera (DP26, Olympus, Germany), and a stereo microscope (ZEISS Axio Zoom.V16, USA) were used to acquire images. ImageJ (National Institute of Health, USA) was used to analyze the acquired images.

As soon as the cell was captured in the droplet, it was rapidly lysed by the lysis buffer in the bead phase and primers on the barcoded bead captured mRNAs. The collected droplets were broken by adding perfluorooctanol (370533-5G, Sigma), and the beads were washed with large volume of 6× saline sodium citrate buffer (SSC) and harvested. The mRNAs were reverse transcribed together to form stable single-cell transcriptomes bonded to beads and then amplified.

Library Construction and Sequencing. Qualified library was built after the completion of DNA fragmentation and cyclization. We used dsDNA fragmentase (M0348L, NEB) to interrupt the target sequence (cDNA) randomly, followed by end-repairing and addition of adapter primers.[24] The fragmented cDNA was amplified with two specific primers. Subsequently, DNA mix was selected to 300−500 bp by AMPure XP beads (Beckman). Finally, the DNA was heat denatured and cyclized into single-strand circular DNA with the aid of exogenous free single-stranded nucleotide primers. We made a DNA nanoball using rolling circle amplification[25,26] and sequenced the resultant molecules from each end using a BGISEQ-500 Sequencer (MGI Tech Co., China). The detailed library construction procedures can be found in Figure S2 and relevant oligonucleotide sequences can be found in Table S1.

Analysis of the scRNA-seq Data. With the obtained paired-end sequencing data, we first converted the data to sam/bam format using Picard (v 2.9.3). We applied Drop-seq tools v 1.13 (ref 15) to decode UMI and cell barcode information embedded in the sequences in order to quantify the transcript abundance. The UMI and cell barcode encoded in Read 1 (forward strand) sequences are abstracted after filtering out low-quality sequences. As for Read 2 (reverse strand) sequences, which were 100 bp mRNA insert sequences, we removed the sequences with high adapter and poly A contamination and used STAR (v 2.5.2b) to map the read sequences to a reference for gene alignment.[11] After quantifying the UMI counts for each cell barcode, we selected cells that have higher number of UMIs (evaluated by "expected cell numbers" or a single "UMI cut-off") as valid cells. In the doublet analysis, the species of the cells were classified if 90% of transcripts were mapped to either of the two species. Cells that had both human and mouse transcripts were regarded as a cell doublet, since it indicated that the primers on the bead simultaneously captured mRNAs from both a human cell and a mouse cell.

Data Availability. The sequencing raw data reported in this study have been deposited to CNGB Nucleotide Sequence Archive (Accession Code: CNP0000223).

RESULTS AND DISCUSSION

Chip Design. This chip was aimed to hydrodynamically focus both cells and beads before droplet generation and encapsulation to improve the encapsulation efficiency. When cells/beads are focused, they align as a train of particles with regular intervals and enter the droplet generating region one by one, reducing the chance of multiple encapsulation.

The microfluidic device adopted spiral and serpentine channels to focus the cells/beads. In spiral channels, due to the viscosity of fluid and velocity imbalance between the channel center and the near-wall region, secondary flow, termed Dean flow, was generated, leading to Dean drag force on the particles. In addition, particles were subjected to lift force, which was the net force of the inertial lift and wall lift, caused by shear gradient and wall lift, respectively.[27,28] The balance of drag force and lift force dictated the equilibrium positions of the particles on the channel cross section.[21] Theoretical studies in inertial microfluidics predicted that particles occupy a single equilibrium position in a curvilinear channel when[27−31]

$$a_p/D_h > 0.07$$

where a_p is the diameter of particles and D_h is the hydraulic diameter. Given that diameters of beads and cells were about 30 and 10 μm, respectively, this requirement could be easily met since usually channel width is below 120 μm. Therefore, in theory both cells and beads can be focused in the channels, though the time it takes to be focused depends on the particle dynamics and lateral migration speed.

Lateral migration speed v can be estimated by[27,28,32]

$$v = \frac{2\rho U_f^2 C_L a_p^3}{3\pi\mu D_h^2}$$

where ρ is the density of the fluid, U_f is the flow velocity of the fluid, μ is the dynamic viscosity of the fluid, and C_L is lift coefficient, which is a function of the particle position on the plane of the channel cross section with an average value of 0.5. It implies that the migration speed scales with a_p^3/D_h^2: smaller-sized cells migrate much more slowly and thus take a longer time to reach the focal positions, which would require longer channels. For example, assuming the widths of the bead channel and the cell channel are 120 and 80 μm, respectively, the migration speed of beads and cells are estimated to be 81.5 and 9.5 μm/s, respectively. To focus cells without employing extremely long spiral channels, an additional focusing mechanism would be beneficial. We adopted serpentine channels[33] at the exit of the spiral channel to facilitate cell focusing, as shown in Figure 1a. In the asymmetrical semicircle serpentine channel, cells were subjected to viscous drag force and centrifugal force, but the time it took to reach an equilibrium position was remarkably reduced.[33,34] As cells and beads line up and approach the droplet generation region, the proportion of multiple encapsulation in single droplets would be reduced and simultaneous encapsulation of single bead and single cell would be increased (Figure 1b).

Our chip design achieved good focusing result. Cells left the spiral channel with a relatively wide range of lateral positions. As they entered the serpentine channel, they were further focused at a position close to the outer wall with reasonably consistent spacing (Figure 1c). Beads were also well-aligned with only the spiral channels, owing to their larger size.

DOI: 10.1021/acssensors.9b00171
ACS Sens. XXXX, XXX, XXX−XXX

Dependence of the Focusing Performance on Cell/Bead Concentration. The cell and bead concentrations are the most immediate factors that affect the downstream encapsulation performance. Higher concentration leads to a higher encapsulation rate, but with a trade-off of higher incidence of multiple encapsulation. To identify the optimal concentrations, we first characterized the effect of cell/bead concentrations on the focusing performance.

We closely examined the distribution of cells/beads' lateral position and spacing in the region before the droplet generator, as defined in Figure 2a, and varied the cell/bead concentrations. We tested three cell concentrations, namely, 350, 650, and 900 μL^{-1}. With the current chip design and flow condition, cells were focused at lateral positions of about 30 μm with full width at half-maximum (fwhm) of about 16 μm in all three cell concentrations (Figure 2b and Figure S3a). A similar observation was acquired for beads under the tested concentrations, namely, 450, 800, and 1100 μL^{-1}: beads were mainly aligned at lateral positions of 40 μm with fwhm of 27 μm in all concentration conditions (Figure 2b and Figure S3b). The observed weak dependence between lateral focusing and cell/bead concentration was likely because in the tested concentrations, the interaction between cell/bead was weak and the dynamics of individual cell/bead was relatively independent.

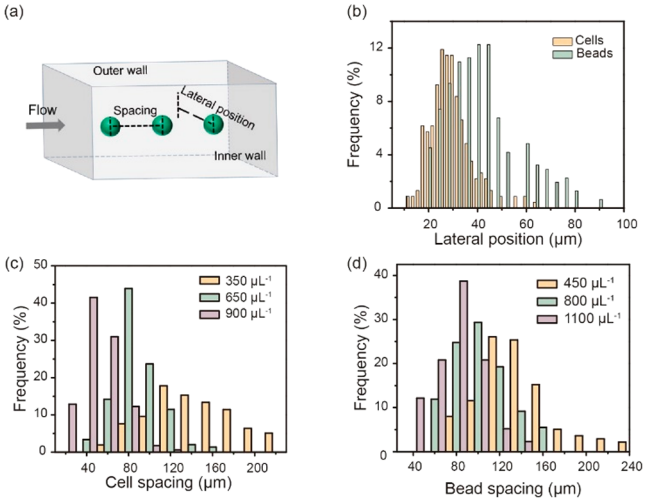

Figure 2. Hydrodynamic focusing of cells and beads. (a) Schematic showing the definition of lateral positions and spacing of cells/beads. (b) Distribution of lateral positions of cells at a concentration of 350 μL^{-1} and beads at a concentration of 450 μL^{-1}. (c) Distribution of spacings between adjacent cells at different cell concentrations as indicated. (d) Distribution of spacings between adjacent beads at different bead concentrations as indicated.

Cell/bead spacing was anticipated to decrease while the cell/bead concentration was increased as the fluids would become more crowded. Indeed, while we increased cell concentration from 350 μL^{-1} to 900 μL^{-1}, the spacing between adjacent cells decreased from 140.9 ± 39.6 μm to 49.8 ± 18.1 μm (Figure 2c). Empirically, cell spacing less than 50 μm posed risks of generating multiple encapsulations. At cell concentration of 350 μL^{-1}, more than 98% of the cells were spaced more than 70 μm away from adjacent cells. As for the beads, while the concentration was increased from 450 to 1100 μL^{-1}, the spacing decreased from 136.0 ± 35.1 μm to 77.7 ± 22.0 μm (Figure 2d). These results verified the capability of this chip design in cell and bead focusing and offered a reference for the following encapsulation experiments.

Encapsulation of Cell and Bead Separately. To achieve efficient cell/bead coencapsulation, it was necessary to encapsulate cell/bead separately with good efficiency. Therefore, we investigated the incidence of single cell/bead and multiple cell/bead encapsulation at varied concentrations (Figure 3).

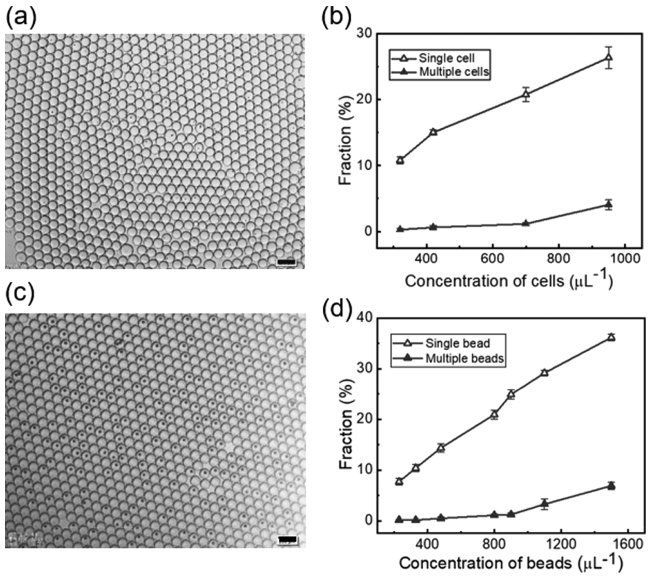

Figure 3. Encapsulation of bead/cell separately at different bead/cell concentrations. (a) Micrograph showing droplets with encapsulated cells when the cells were flowed at a concentration of 700 μL^{-1}. (b) Fraction of droplets encapsulated with single or multiple cells at different cell concentrations. (c) Micrograph showing droplets with encapsulated beads when beads were flowed at a concentration of 900 μL^{-1}. (d) Fraction of droplets encapsulated with single or multiple beads at different cell concentrations. Scale bars, 200 μm. Data represents mean ± standard deviation with n = 3.

As expected, the fractions of both single cell and multiple cell encapsulation increased as we increased the cell concentration. As shown in Figure 3b, when the cell concentration was 320 μL^{-1}, the fraction of single and multiple encapsulation was 10.68 ± 0.48% and 0.36 ± 0.07%, respectively. As we increased the cell concentration to 700 μL^{-1}, the fraction of single cell encapsulation was almost doubled, namely, 20.77 ± 1.07%, while the fraction of multiple cell encapsulation showed a 3-fold increase, with a value of 1.15 ± 0.20%. As we increased the concentration further, though the fraction of single cell encapsulation increased at a relatively constant pace, the incidence of multiple encapsulation increased rapidly. At 900 μL^{-1}, the fraction of multiple encapsulation had reached 4.06 ± 0.75%, with almost a 4-fold increase compared to that at 700 μL^{-1}. Given this observed trade-off between single and multiple encapsulation, it was beneficial to keep the cell concentration lower than 700 μL^{-1}.

Similar observation was obtained in the experiments with beads. The fraction of single bead encapsulation increased at a relatively consistent rate as we increased the concentration, but the fraction of multiple encapsulation started to increase quickly at 900 μL^{-1}, where the fraction of single and multiple encapsulation was 24.88 ± 0.92% and 1.22 ± 0.27%, respectively, as shown in Figure 3d. The detailed experimental

DOI: 10.1021/acssensors.9b00171
ACS Sens. XXXX, XXX, XXX−XXX

data can be found in Supporting Information Tables S2 and S3.

Coencapsulation of Beads and Cells. We loaded both bead and cell suspensions into the device and tested the cell/bead coencapsulation performance. Based on the observation in the experiments of separate encapsulation, we adopted a bead concentration of 900 μL^{-1}, under which condition 25% of the overall droplets were single encapsulation and the incidence of multiple incidence was only 1.2%. To minimize the presence of cell doublets, we used a relatively low cell concentration of 300 μL^{-1}, which would still give a reasonable fraction of separate encapsulation of about 10% (see Figure 3b) and a low doublet fraction of about 0.3%. The resultant coencapsulation rate should be 25% × 10% = 2.5% assuming the encapsulation of cells and beads are independent incidence.

We aimed to compare the performance of our device with that of Drop-seq device and the device which only focused beads (ref 21). Since detailed characterization of the encapsulation performance of the Drop-seq device was not available in the literature and the documentation of Drop-seq protocols was easily accessible, we performed experiments using the Drop-seq device. Performance of the other device was based on its published data.

We defined effective encapsulation as the simultaneous encapsulation of one cell and one bead and false encapsulation as simultaneous encapsulation of one cell and multiple beads, multiple cells and one bead, and multiple cells and multiple beads. The percentage of effective encapsulation in the overall generated droplets reflects the coencapsulation efficiency. In our device, which incorporated double focusing channels, 2.93 ± 0.29% of the droplets were effective droplets, which was about 2-fold the fraction of 1.63 ± 0.19% in the Drop-seq device with no focusing channels, as shown in Figure 4a-c. The fraction of false encapsulation in our device, which was 0.24 ± 0.08%, was also almost one-third of that in Drop-seq, which was 0.65 ± 0.095%. These results suggested that our device could significantly improve the performance of Drop-seq. It was noticed that the percentage of effective encapsulation was also close to the aforementioned estimation of 2.5%.

In the reported work using a single focusing channel, with a cell concentration of 250 μL^{-1} and a bead concentration of 1000 μL^{-1}, the fraction of effective encapsulation among effective and false encapsulation combined was 95%. In our case, the value was 92.4%, which was close but slightly lower, presumably because of the slightly different cell and bead concentrations used and fluid driving mechanism.

Cell utilization rate and throughput were adopted as two additional metrics to characterize the performance. Cell utilization rate, defined as the percentage of effective encapsulated cells in the total cells dispensed into the device, reflected the cell capturing efficiency. Throughput was defined as the number of effective encapsulations generated per minute. Not surprisingly, our device showed significantly improved cell utilization rate and throughput compared to Drop-seq, as shown in Figure 4d. The cell utilization rate was 28.65 ± 3.54% in our case, which was roughly a 4-fold increase of the 7.05 ± 0.49% in Drop-seq. Throughput was improved from the 126.9 ± 8.6 min^{-1} in Drop-seq to the 519.0 ± 58 min^{-1} in our device.

The reported cell utilization rate and throughput using single focusing channel (defined as cell yield) was 20% and 2700 min^{-1} at cell concentration of 250 μL^{-1} and bead concentration of 1000 μL^{-1}. Our device outperformed the

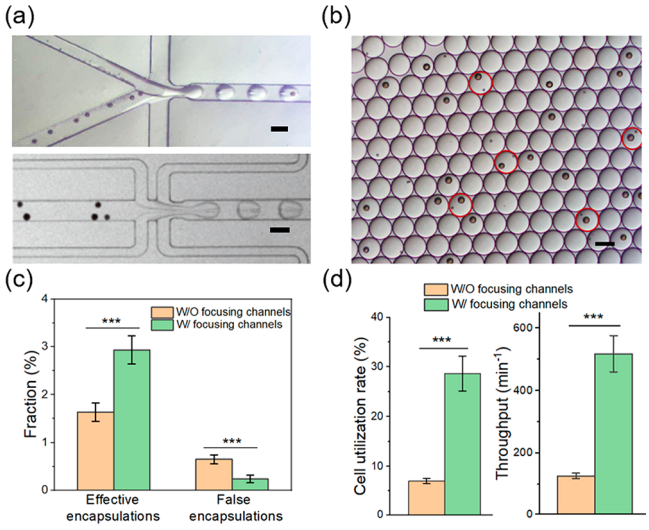

Figure 4. Coencapsulation of beads and cells using the designed chip and traditional Drop-seq chip. (a) Micrographs showing the bead and cell locations near the encapsulation region using the designed chip with focusing channels and traditional Drop-seq device without focusing channels. Upper: the designed chip with focusing channels; lower: Drop-seq devices without focusing channels. Scale bars, 100 μm. (b) Micrograph showing the resultant droplets. Circled droplets represent effective encapsulations, where a single cell and a single bead were simultaneously encapsulated. Scale bar, 100 μm. (c) Fractions of effective encapsulation and false encapsulations using the indicated devices. False encapsulation was defined as encapsulation of one bead and multiple cells, one cell and multiple beads, or multiple cells and multiple beads. (d) Cell utilization rate and throughput using the indicated devices. Cell utilization rate was defined as the fraction of the total infused cells that were effectively encapsulated. Throughput was defined as the amount of effective encapsulations generated per minute. Data represents mean ± standard deviation with $n = 3$. ***, $P < 0.001$.

device using a single focusing channel in terms of cell utilization with a 40% increase, which suggested that while the cells were ordered, the encapsulation efficiency was improved and fewer cells were wasted. As for throughput, since we used negative pressure for fluids dispensing and the volume flow rates were much smaller, our device showed a disadvantage, with a throughput five times lower than the reported value. Nevertheless, more than 5000 effective encapsulations were collected in 10 min runs.

scRNA-seq with Human and Mouse Cell Mixture. To validate the utility of this microfluidic platform, we used cell mixtures from two cell lines, namely, human HEK293T and mouse NIH3T3, and performed cell/bead coencapsulation and downstream expression profiling, using our device as well as the Drop-seq device for comparison. Cell suspensions were loaded at a concentration of 300 μL^{-1} and barcoded beads at 900 μL^{-1}. Upon encapsulation, cells were lysed and mRNA were captured by the barcoded beads. Droplets were collected into a tube for 25 min and then coalesced, and the mRNAs captured on the barcoded beads were subsequently reverse transcribed and amplified, before the constructed library was sequenced. On average, 8047 UMIs per human cell and 5146 UMIs per mouse cell were detected, which was consistent with the reported values and validated the sequencing results (Figure S4).

Following the similar practice as Drop-seq, we evaluated the incidence of doublets from the sequenced data, as shown in

DOI: 10.1021/acssensors.9b00171
ACS Sens. XXXX, XXX, XXX−XXX

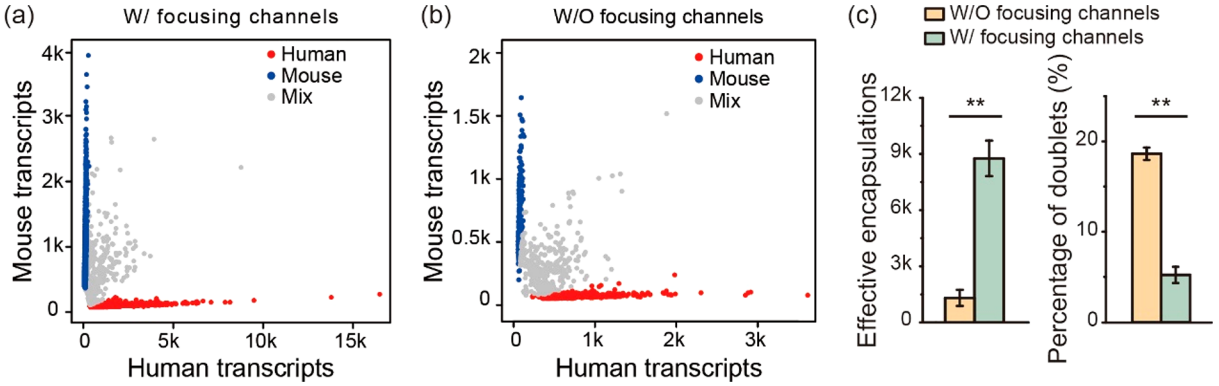

Figure 5. Comparison of the sequencing data obtained from devices with and without focusing channels. (a and b) Species plot based on the analyzed transcripts from the sequencing results. Each scattered dot represents the read from a barcoded bead, being classified as single human cell, single mouse cell, or mix, as indicated. The loaded concentration of cells and beads were 300 and 900 μL^{-1}, respectively. (c) Amount of effective encapsulations and the percentage of doublets analyzed from the sequencing data. Data represents mean ± standard deviation with $n = 3$. **, $P < 0.01$.

Figure 5a and b. In the collected sample, transcripts from 8760 ± 951 single cell encapsulations were recovered from the sequencing data, which was significantly higher than using the Drop-seq device, the data from which recovered only 1313 ± 430 single cell encapsulations (Figure 5c). The percentage of doublets in the sequencing data was 5.22 ± 0.90%, which was also significantly lower than the 18.63 ± 0.68% in the data using the Drop-seq device (Figure 5c). These results suggested that our device design greatly improved the performance of single cell capture and library preparation. The doublet fraction could be further reduced by lowering the cell concentration. We tested the cell concentration of 150 μL^{-1} while maintaining other conditions; a doublet fraction of 1.7% was achieved (Figure S5). It was noticed that the reported doublet fraction using the device with single focusing channel was 2.2% at the cell concentration of 250 μL^{-1}, which was comparable to the performance of our device in this regard.

CONCLUSION

In this work, we presented a microfluidic design with improved performance for single-cell expression profiling. We adopted spiral and serpentine channels to focus beads and cells, resulting in ordered beads and cells flows, which reduced the incidence of multiple encapsulation and increased cell utilization rate. Results showed that the newly designed device improved the cell utilization rate by 4-fold compared to Drop-seq device; compared to the device that focused beads alone, the cell utilization rate was enhanced by 40%. Sequencing results also confirmed the performance improvement compared to Drop-seq. This platform displayed great potential for the application of single cell analysis where samples are scarce.

ASSOCIATED CONTENT

Supporting Information

The Supporting Information is available free of charge on the ACS Publications website at DOI: 10.1021/acssensors.9b00171.

Chip dimension and the experimental platform, library construction, lateral position of cells and beads under three different concentrations, respectively, relevant oligonucleotide sequences, encapsulation rates at different bead/cell concentrations, violin plots of UMIs per cell using new designed chip under cell concentration of 300 μL^{-1} and bead concentration of 900 μL^{-1}, and sequencing results using the designed chip at a lower cell concentration of 150 μL^{-1} (PDF)

AUTHOR INFORMATION

Corresponding Authors

*E-mail: zidali@szu.edu.cn.
*E-mail: heliqun@ustc.edu.cn.

ORCID

Weiping Ding: 0000-0002-3331-1011
Liqun He: 0000-0002-5857-0490

Author Contributions

#Luoquan Li and Ping Wu contributed equally to this work.

Notes

The authors declare no competing financial interest.

ACKNOWLEDGMENTS

The authors thank Shichen Dong, Yongtian Zhao, Yue Yuan, and Taiqing Feng for the help with fluidic experiments, sequencing, and data analysis. This study was supported by the National Natural Science Foundation of China (Grant No. 31500694, 31670866, and 31570755) and Shenzhen Peacock Talent Plan (No. KQTD20150330171505310).

REFERENCES

(1) Meacham, C. E.; Morrison, S. J. Tumour heterogeneity and cancer cell plasticity. *Nature* **2013**, *501* (7467), 328−37.
(2) Aw Yong, K. M.; Li, Z.; Merajver, S. D.; Fu, J. Tracking the tumor invasion front using long-term fluidic tumoroid culture. *Sci. Rep.* **2017**, *7* (1), 10784.
(3) Mardis, E. R. Next-generation DNA sequencing methods. *Annu. Rev. Genomics Hum. Genet.* **2008**, *9*, 387−402.
(4) Wu, A. R.; Neff, N. F.; Kalisky, T.; Dalerba, P.; Treutlein, B.; Rothenberg, M. E.; Mburu, F. M.; Mantalas, G. L.; Sim, S.; Clarke, M. F.; Quake, S. R. Quantitative assessment of single-cell RNA-sequencing methods. *Nat. Methods* **2014**, *11* (1), 41−6.
(5) Hashimshony, T.; Senderovich, N.; Avital, G.; Klochendler, A.; de Leeuw, Y.; Anavy, L.; Gennert, D.; Li, S.; Livak, K. J.; Rozenblatt-Rosen, O.; Dor, Y.; Regev, A.; Yanai, I. CEL-Seq2: sensitive highly-multiplexed single-cell RNA-Seq. *Genome Biol.* **2016**, *17*, 77.
(6) Harris, R. A.; Wang, T.; Coarfa, C.; Nagarajan, R. P.; Hong, C.; Downey, S. L.; Johnson, B. E.; Fouse, S. D.; Delaney, A.; Zhao, Y.; Olshen, A.; Ballinger, T.; Zhou, X.; Forsberg, K. J.; Gu, J.; Echipare, L.; O'Geen, H.; Lister, R.; Pelizzola, M.; Xi, Y.; Epstein, C. B.;

DOI: 10.1021/acssensors.9b00171
ACS Sens. XXXX, XXX, XXX−XXX

Bernstein, B. E.; Hawkins, R. D.; Ren, B.; Chung, W. Y.; Gu, H.; Bock, C.; Gnirke, A.; Zhang, M. Q.; Haussler, D.; Ecker, J. R.; Li, W.; Farnham, P. J.; Waterland, R. A.; Meissner, A.; Marra, M. A.; Hirst, M.; Milosavljevic, A.; Costello, J. F. Comparison of sequencing-based methods to profile DNA methylation and identification of monoallelic epigenetic modifications. *Nat. Biotechnol.* **2010**, *28* (10), 1097−105.

(7) Adler, A. S.; Mizrahi, R. A.; Spindler, M. J.; Adams, M. S.; Asensio, M. A.; Edgar, R. C.; Leong, J.; Leong, R.; Johnson, D. S. Rare, high-affinity mouse anti-PD-1 antibodies that function in checkpoint blockade, discovered using microfluidics and molecular genomics. *MAbs* **2017**, *9* (8), 1270−1281.

(8) Ma, X.; Liu, Y.; Liu, Y.; Alexandrov, L. B.; Edmonson, M. N.; Gawad, C.; Zhou, X.; Li, Y.; Rusch, M. C.; Easton, J.; Huether, R.; Gonzalez-Pena, V.; Wilkinson, M. R.; Hermida, L. C.; Davis, S.; Sioson, E.; Pounds, S.; Cao, X.; Ries, R. E.; Wang, Z.; Chen, X.; Dong, L.; Diskin, S. J.; Smith, M. A.; Guidry Auvil, J. M.; Meltzer, P. S.; Lau, C. C.; Perlman, E. J.; Maris, J. M.; Meshinchi, S.; Hunger, S. P.; Gerhard, D. S.; Zhang, J. Pan-cancer genome and transcriptome analyses of 1,699 paediatric leukaemias and solid tumours. *Nature* **2018**, *555* (7696), 371−376.

(9) Dal Molin, A.; Di Camillo, B. How to design a single-cell RNA-sequencing experiment: pitfalls, challenges and perspectives. *Briefings Bioinf.* **2018**, DOI: 10.1093/bib/bby007.

(10) Xu, Y.; Zhou, X. Applications of Single-Cell Sequencing for Multiomics. *Methods Mol. Biol.* **2018**, *1754*, 327−374.

(11) Hwang, B.; Lee, J. H.; Bang, D. Single-cell RNA sequencing technologies and bioinformatics pipelines. *Exp. Mol. Med.* **2018**, *50* (8), 96.

(12) Ziegenhain, C.; Vieth, B.; Parekh, S.; Reinius, B.; Guillaumet-Adkins, A.; Smets, M.; Leonhardt, H.; Heyn, H.; Hellmann, I.; Enard, W. Comparative Analysis of Single-Cell RNA Sequencing Methods. *Mol. Cell* **2017**, *65* (4), 631−643.e4.

(13) Kakaradov, B.; Arsenio, J.; Widjaja, C. E.; He, Z.; Aigner, S.; Metz, P. J.; Yu, B.; Wehrens, E. J.; Lopez, J.; Kim, S. H.; Zuniga, E. I.; Goldrath, A. W.; Chang, J. T.; Yeo, G. W. Early transcriptional and epigenetic regulation of CD8(+) T cell differentiation revealed by single-cell RNA sequencing. *Nat. Immunol.* **2017**, *18* (4), 422−432.

(14) Azizi, E.; Carr, A. J.; Plitas, G.; Cornish, A. E.; Konopacki, C.; Prabhakaran, S.; Nainys, J.; Wu, K.; Kiseliovas, V.; Setty, M.; Choi, K.; Fromme, R. M.; Dao, P.; McKenney, P. T.; Wasti, R. C.; Kadaveru, K.; Mazutis, L.; Rudensky, A. Y.; Pe'er, D. Single-Cell Map of Diverse Immune Phenotypes in the Breast Tumor Microenvironment. *Cell* **2018**, *174* (5), 1293−1308.e36.

(15) Macosko, E. Z.; Basu, A.; Satija, R.; Nemesh, J.; Shekhar, K.; Goldman, M.; Tirosh, I.; Bialas, A. R.; Kamitaki, N.; Martersteck, E. M.; Trombetta, J. J.; Weitz, D. A.; Sanes, J. R.; Shalek, A. K.; Regev, A.; McCarroll, S. A. Highly Parallel Genome-wide Expression Profiling of Individual Cells Using Nanoliter Droplets. *Cell* **2015**, *161* (5), 1202−1214.

(16) Klein, A. M.; Mazutis, L.; Akartuna, I.; Tallapragada, N.; Veres, A.; Li, V.; Peshkin, L.; Weitz, D. A.; Kirschner, M. W. Droplet barcoding for single-cell transcriptomics applied to embryonic stem cells. *Cell* **2015**, *161* (5), 1187−1201.

(17) Hosokawa, M.; Nishikawa, Y.; Kogawa, M.; Takeyama, H. Massively parallel whole genome amplification for single-cell sequencing using droplet microfluidics. *Sci. Rep.* **2017**, *7* (1), 5199.

(18) Habib, N.; Avraham-Davidi, I.; Basu, A.; Burks, T.; Shekhar, K.; Hofree, M.; Choudhury, S. R.; Aguet, F.; Gelfand, E.; Ardlie, K.; Weitz, D. A.; Rozenblatt-Rosen, O.; Zhang, F.; Regev, A. Massively parallel single-nucleus RNA-seq with DroNc-seq. *Nat. Methods* **2017**, *14* (10), 955−958.

(19) Zhang, J.; Yan, S.; Yuan, D.; Alici, G.; Nguyen, N. T.; Ebrahimi Warkiani, M.; Li, W. Fundamentals and applications of inertial microfluidics: a review. *Lab Chip* **2016**, *16* (1), 10−34.

(20) Choi, J.; Hong, S. C.; Kim, W.; Jung, J. H. Highly Enriched, Controllable, Continuous Aerosol Sampling Using Inertial Microfluidics and Its Application to Real-Time Detection of Airborne Bacteria. *ACS Sens* **2017**, *2* (4), 513−521.

(21) Moon, H. S.; Je, K.; Min, J. W.; Park, D.; Han, K. Y.; Shin, S. H.; Park, W. Y.; Yoo, C. E.; Kim, S. H. Inertial-ordering-assisted droplet microfluidics for high-throughput single-cell RNA-sequencing. *Lab Chip* **2018**, *18* (5), 775−784.

(22) Li, Z.; Mak, S. Y.; Sauret, A.; Shum, H. C. Syringe-pump-induced fluctuation in all-aqueous microfluidic system implications for flow rate accuracy. *Lab Chip* **2014**, *14* (4), 744−9.

(23) Mak, S. Y.; Li, Z.; Frere, A.; Chan, T. C.; Shum, H. C. Musical interfaces: visualization and reconstruction of music with a microfluidic two-phase flow. *Sci. Rep.* **2015**, *4*, 6675.

(24) Huang, J.; Liang, X.; Xuan, Y.; Geng, C.; Li, Y.; Lu, H.; Qu, S.; Mei, X.; Chen, H.; Yu, T.; Sun, N.; Rao, J.; Wang, J.; Zhang, W.; Chen, Y.; Liao, S.; Jiang, H.; Liu, X.; Yang, Z.; Mu, F.; Gao, S. A reference human genome dataset of the BGISEQ-500 sequencer. *GigaScience* **2017**, *6* (5), 1−9.

(25) Drmanac, R.; Sparks, A. B.; Callow, M. J.; Halpern, A. L.; Burns, N. L.; Kermani, B. G.; Carnevali, P.; Nazarenko, I.; Nilsen, G. B.; Yeung, G.; Dahl, F.; Fernandez, A.; Staker, B.; Pant, K. P.; Baccash, J.; Borcherding, A. P.; Brownley, A.; Cedeno, R.; Chen, L.; Chernikoff, D.; Cheung, A.; Chirita, R.; Curson, B.; Ebert, J. C.; Hacker, C. R.; Hartlage, R.; Hauser, B.; Huang, S.; Jiang, Y.; Karpinchyk, V.; Koenig, M.; Kong, C.; Landers, T.; Le, C.; Liu, J.; McBride, C. E.; Morenzoni, M.; Morey, R. E.; Mutch, K.; Perazich, H.; Perry, K.; Peters, B. A.; Peterson, J.; Pethiyagoda, C. L.; Pothuraju, K.; Richter, C.; Rosenbaum, A. M.; Roy, S.; Shafto, J.; Sharanhovich, U.; Shannon, K. W.; Sheppy, C. G.; Sun, M.; Thakuria, J. V.; Tran, A.; Vu, D.; Zaranek, A. W.; Wu, X.; Drmanac, S.; Oliphant, A. R.; Banyai, W. C.; Martin, B.; Ballinger, D. G.; Church, G. M.; Reid, C. A. Human genome sequencing using unchained base reads on self-assembling DNA nanoarrays. *Science* **2010**, *327* (5961), 78−81.

(26) Fehlmann, T.; Reinheimer, S.; Geng, C.; Su, X.; Drmanac, S.; Alexeev, A.; Zhang, C.; Backes, C.; Ludwig, N.; Hart, M.; An, D.; Zhu, Z.; Xu, C.; Chen, A.; Ni, M.; Liu, J.; Li, Y.; Poulter, M.; Li, Y.; Stahler, C.; Drmanac, R.; Xu, X.; Meese, E.; Keller, A. cPAS-based sequencing on the BGISEQ-500 to explore small non-coding RNAs. *Clin. Epigenet.* **2016**, *8*, 123.

(27) Ramachandraiah, H.; Ardabili, S.; Faridi, A. M.; Gantelius, J.; Kowalewski, J. M.; Martensson, G.; Russom, A. Dean flow-coupled inertial focusing in curved channels. *Biomicrofluidics* **2014**, *8* (3), 034117.

(28) Kemna, E. W.; Schoeman, R. M.; Wolbers, F.; Vermes, I.; Weitz, D. A.; van den Berg, A. High-yield cell ordering and deterministic cell-in-droplet encapsulation using Dean flow in a curved microchannel. *Lab Chip* **2012**, *12* (16), 2881−7.

(29) Hasni, A. E.; Göbbels, K.; Thiebes, A. L.; Bräunig, P.; Mokwa, W.; Schnakenberg, U. Focusing and Sorting of Particles in Spiral Microfluidic Channels. *Procedia Eng.* **2011**, *25*, 1197−1200.

(30) Nivedita, N.; Ligrani, P.; Papautsky, I. Dean Flow Dynamics in Low-Aspect Ratio Spiral Microchannels. *Sci. Rep.* **2017**, *7*, 44072.

(31) Xiang, N.; Ni, Z.; Yi, H. Concentration-controlled particle focusing in spiral elasto-inertial microfluidic devices. *Electrophoresis* **2018**, *39* (2), 417−424.

(32) Bhagat, A. A. S.; Kuntaegowdanahalli, S. S.; Papautsky, I. Inertial microfluidics for continuous particle filtration and extraction. *Microfluid. Nanofluid.* **2009**, *7* (2), 217−226.

(33) Di Carlo, D.; Irimia, D.; Tompkins, R. G.; Toner, M. Continuous inertial focusing, ordering, and separation of particles in microchannels. *Proc. Natl. Acad. Sci. U. S. A.* **2007**, *104* (48), 18892−7.

(34) Wang, L.; Dandy, D. S. High-Throughput Inertial Focusing of Micrometer- and Sub-Micrometer-Sized Particles Separation. *Adv. Sci. (Weinh)* **2017**, *4* (10), 1700153.

DOI: 10.1021/acssensors.9b00171
ACS Sens. XXXX, XXX, XXX−XXX